Flow modeling of linear and nonlinear fluids in two scale fibrous fabrics

Elena Lopez, Adrien Leygue, Emmanuelle Abisset-Chavanne, Sébastien Comas-Cardona, Christophe Aufrere, Christophe Binetruy, Francisco Chinesta

Flow modeling of linear and nonlinear fluids in two scale fibrous fabrics

Advanced simulations

Elena Lopez[1], Adrien Leygue[1], Emmanuelle Abisset-Chavanne[1], Sebastien Comas-Cardona[1], Christophe Aufrere[2], Christophe Binetruy[1], Francisco Chinesta[1]

Abstract The fundamental macroscopic material property needed to quantify the flow in a fibrous medium viewed as a porous medium is the permeability. Composite processing models require the permeability as input data to predict flow patterns and pressure fields. As permeability reflects both the magnitude and anisotropy of the fluid/fiber resistance, efficient numerical techniques are needed to solve linear and nonlinear homogenization problems online during the flow simulation. In a previous work the expressions of macroscopic permeability were derived in a double-scale porosity medium for both Newtonian and rheo-thinning resins. In the linear case only a microscopic calculation on a representative volume is required, implying as many microscopic calculations as representative microscopic volumes exist in the whole fibrous structure. In the non-linear case, and even when the porous microstructure can be described by a unique representative volume, microscopic calculation must be carried out many times because the microscale resin viscosity depends on the macroscopic velocity, which in turn depends on the permeability that results from a microscopic calculation. Thus, a nonlinear multi-scale problem results. In this paper an original and efficient offline-online procedure is proposed for the efficient solution of nonlinear flow problems in porous media.

Keywords Permeability · Computational homogenization · Nonlinear fluids · Composite materials · Model order reduction · Proper generalized decomposition · Parametric solutions · Computational vademecums

✉ Francisco Chinesta
Francisco.Chinesta@ec-nantes.fr

Elena Lopez
Elena.Lopez-Tomas@ec-nantes.fr

Adrien Leygue
Adrien.Leygue@ec-nantes.fr

Emmanuelle Abisset-Chavanne
Emmanuelle.Abisset-Chavanne@ec-nantes.fr

Sebastien Comas-Cardona
Sebastien.Comas@ec-nantes.fr

Christophe Aufrere
christophe.aufrere@faurecia.com

Christophe Binetruy
Christophe.Binetruy@ec-nantes.fr

[1] GeM UMR CNRS-Centrale Nantes, 1 rue de la Noe, 44300 Nantes, France

[2] Faurecia Group, 2 rue Hennape, 92000 Nanterre, France

Introduction

Suppose a composite material occupying the domain $\Omega \in \mathbb{R}^d$, $d \leq 3$, in which a flow problem is considered and the velocity field $\mathbf{v}(\mathbf{X}, t)$, $\mathbf{X} \in \Omega$ searched at each time $t \in (0, \mathcal{T}]$. The domain Ω is assumed fully saturated, with the fluid phase occupying the region Ω_f whereas the remaining part $\Omega_s = \Omega - \Omega_f$ is occupied by a solid phase assumed at rest, i.e. $\mathbf{v}(\mathbf{X} \in \Omega_s) = \mathbf{0}$ and rigid enough.

Considering a Newtonian fluid and neglecting the inertia terms, the flow is described by the Stokes model defined in Ω_f:

$$\begin{cases} \nabla p(\mathbf{X}) = \eta \nabla^2 \mathbf{v}(\mathbf{X}) \\ \nabla \cdot \mathbf{v}(\mathbf{X}) = 0 \end{cases} \tag{1}$$

where p is the pressure field, $\mathbf{v}$ the velocity field and η the fluid viscosity.

The solution of this problem requires to impose adequate boundary conditions on $\partial\Omega$, that are enforced in the solution process in a standard way. There is a variety of discretization techniques for solving numerically such a flow problem. The interested reader can refer to [7] and the numerous references therein.

The description of internal structure of heterogeneous materials at a variety of length scales needs a resolution high enough for capturing the size, orientation and distribution of the material constituents (heterogeneity) and then its effects on the velocity field. Fibrous media with a large number of fibers and inter-fiber volumes cannot be described by considering each of the fibers (viewed as heterogeneities here) or interfiber volumes, which would lead to intractable boundary value problems to solve for the flow. Then, another continuum approach at a coarser level is required. One possibility consists of separating the scales (when it can be performed) and associate to each point $\mathbf{X} \in \Omega$ a representative volume at the finest scale $\omega(\mathbf{X})$ (with boundary $\partial\omega(\mathbf{X})$) where homogenization is carried out.

When the same physics is valid and applies at each scale, for example in the case of thermo-mechanical models, homogenization procedures work quite well in both the linear and the nonlinear case. Linear and nonlinear thermo-mechanical homogenization is the subject of many researches, including its computational counterpart, over the last three decades. The interested reader can refer to [8, 14, 15] and the references therein. The main issue in computational homogenization is the consideration of nonlinear behaviors that require many costly calculations. The use of model order reduction techniques is an appealing route for improving the efficiency of multi-scale solvers [3, 11, 12].

In the case of flows in porous media, the macroscopic scale corresponds to the scale of the part, much bigger than the heterogeneities scale, whereas the microscopic one coincides with the scale of heterogeneities. It is well known that in these circumstances for a linear fluid the macroscopic behavior is well described by the phenomenological Darcy's law relating the fluid velocity and the pressure gradient at the macroscopic scale, whereas at the microscopic level the flow behavior is described by the Stokes problem defined in the domain occupied by the fluid (in this work for the sake of simplicity we consider the solid phase rigid and at rest).

Even if both descriptions are notably different, appropriate bridges can be defined to associate to each point $\mathbf{X}$ in Ω a permeability tensor $\mathbf{K}(\mathbf{X})$ relating locally the equivalent macroscopic velocity $\mathbf{V}(\mathbf{X})$ and the pressure gradient $\nabla P(\mathbf{X})$, by upscaling the microscopic physics that only involves as material parameter the fluid viscosity η.

In [13] we derived the expressions of the macroscopic permeability in a double-scale porosity medium for both Newtonian and rheo-thinning fluids. In the linear case only a microscopic calculation on a representative volume is required, which implies as many microscopic calculations as representative microscopic volumes exist in Ω. The amount of computations is then related to the local gradients of the inter-fiber space in the considered fibrous medium. That computational effort can be high for non-homogeneous fibrous structures whith spatial variance in inter-fiber space. In the non-linear case, and even when the microstructure can be described by a unique representative volume, the microscopic calculation must be carried out many times because the microscale resin viscosity depends on the macroscopic velocity, which in turn depends on the macroscopic permeability obtained from the microscopic calculation. In this work an original and efficient offline-online procedure is proposed that allows solving the multi-scale nonlinear problem described above with the computational cost characteristic of a macroscopic nonlinear solution. This procedure is based on the calculation of the microscopic parametric solution, given the velocity field at each point in the representative volume $\omega(\mathbf{X})$, $\mathbf{v}(\mathbf{x} \in \omega(\mathbf{X}))$, for any value of the macroscopic velocity field $\mathbf{V}$, $\mathbf{v}(\mathbf{x} \in \omega(\mathbf{X}); \mathbf{V})$. It allows to compute the permeability of the representative volume for each macroscopic velocity, that is, for any flow rate through it, $\mathbf{K}(\mathbf{V})$.

For computing such a parametric solution one could follow the so-called "brute force approach" that consists of identifying all the possible values of the macroscopic velocity vector $\mathbf{V}$, whose simplest representation implies the angular discretization and also the one related to its norm. In the 2D case, that is the usual framework when addressing liquid composites moulding, the velocity at each position $\mathbf{X}$ in the part, $\mathbf{V}$, can be represented as $\mathbf{V}^T = \|\mathbf{V}\|(\cos\theta, \sin\theta) = V(\cos\theta, sin\theta))$. Suppose that $V \in \mathcal{V}$ and $\theta \in \Theta = [0, 2\pi)$, with the former, $\mathcal{V}$, defined by the user depending on the process knowledge. Now we consider different values of V, $V_i \in \mathcal{V}$, $i = 1, \cdots, N_V$ and N_θ values $\theta_j \in \Theta$, $j = 1, \cdots, N_\theta$, and compute for each couple (i, j), that is, for each velocity $\mathbf{V}^T_{i,j} = V_i(\cos\theta_j, \sin\theta_j)$, a microscopic problem that will be defined in the next section. Thus, $N_V \times N_\theta$ calculations must be performed at each representative volume $\omega(\mathbf{X}_k)$, $k = 1, \cdots, N_X$. This conceptually simple approach requires the solution of $N_X \times N_V \times N_\theta$ nonlinear boundary value problems – BVP – with the corresponding computational cost. If we assume that the nonlinearity requires on average the solution of N_{NL} iterations, the total number of BVP to be solved scales with $N_{NL} \times N_X \times N_V \times N_\theta$, the complexity of each one scaling with the number of degrees of freedom considered for discretizing the microscopic velocity field (in our 2D case twice the number of nodes used for approximating the microscopic velocity field). The "brut force approach" seems definitively conceptually simple but computationally too expensive, even if it always allows to compute offline any possible scenario that might be found online.

Thus, knowing $\mathbf{v}(\mathbf{x} \in \omega(\mathbf{X}_k); V_i, \theta_j)$, $\forall k, i, j$, as soon as the calculation at the macroscopic scale and at a certain iteration of the nonlinear solver requires the value of $\mathbf{K}(\mathbf{X})$, one could proceed as follows:

- Identify the representative volume $\omega(\mathbf{X}_k)$ that corresponds to the microstructure existing at position $\mathbf{X}$;
- Identify the closest velocity $\mathbf{V}_{i,j}$ to the existing macroscopic velocity at position $\mathbf{X}$, $\mathbf{V}(\mathbf{X})$;
- Associate to $\mathbf{X}$, the microscopic velocity field $\mathbf{v}(\mathbf{x} \in \omega(\mathbf{X}_k), V_i, \theta_j)$;
- The permeability $\mathbf{K}(\mathbf{X})$ derives from that microscopic velocity fields as described later.

The determination of the closest velocity can be substituted by a more accurate interpolation. In any case, in the online phase the complexity that arises from microscopic calculations to solve for a 2D nonlinear problem reduces to simple particularizations or interpolations from the pre-computed parametric solution.

The main aim of this study is not to reduce the online computing time. It actually aims at reducing the offline computational cost by reducing significantly the number of BVP to be solved. For that purpose, and for a given representative volume $\omega(\mathbf{X}_k)$, we would like to compute the solution without the necessity of solving a problem for each couple (i, j), (V_i, θ_j). To this end different strategies could be envisaged. One among them, proceeds by constructing a surrogate model. To do so the model is solved in few locations (using an adequate sampling strategy) and the solution is interpolated to any other point (using an appropriate interpolation scheme, e.g. Kriging [10]). The main drawback is that both the sampling and the interpolation must be accurate enough, and it is a priori difficult to conclude on both performances. Other possibility consists of using all the recent technology associated to parametric problems in the framework of model order reduction methods. For a complete description the reader can refer to [6] and the references therein.

This work investigates a particular route based on the use of the so-called Proper Generalized Decomposition – PGD – widely described in our recent works [4, 6]. The main idea of the PGD technique, when focusing on a given microstructure $\omega(\mathbf{X}_k)$, consists of introducing the parameters as extra-coordinates and then solving the resulting multidimensional problem by using a separated representation of the problem solution for circumventing the curse of dimensionality that high dimensional models entail. In the case here considered the microscopic parametric velocity field, within the PGD framework, reads:

$$v_m(\mathbf{x} \in \omega(\mathbf{X}_k), \mathbf{V}) \approx \sum_{n=1}^{Q} R_n^m(\mathbf{x}) \cdot S_n^m(\mathbf{V}) \tag{2}$$

for $m = 1, 2$. This expression can be written in a more compact form as

$$\mathbf{v}(\mathbf{x} \in \omega(\mathbf{X}_k), \mathbf{V}) \approx \sum_{n=1}^{Q} \mathbf{R}_n(\mathbf{x}) \circ \mathbf{S}_n(\mathbf{V}) \tag{3}$$

where the symbol " $\circ$ " denotes the Hadamard product.

By using this computational route for calculating the parametric solution, instead of solving $N_V \times N_\theta$ nonlinear BVP we must solve much less problems as described later.

The next section revisits the main elements related to the micro-to-macro upscaling leading to the definition of an equivalent macroscopic permeability. Then, in Section "Advanced nonlinear Stokes' solver" the construction of a parametric solution related to each representative volume within the PGD framework is addressed. Finally Section "Numerical results" shows some numerical results to demonstrate the potential of the proposed approach.

Revisiting computational homogenization of two-scale flows of linear and nonlinear fluids

In this section the expressions of the macroscopic permeability for both linear and nonlinear fluids are derived.

Linear fluids

Without loss of generality, suppose a statistically homogenous porous medium where two characteristic scales coexist, the coarsest one in Ω and the finest in ω (for the sake of simplicity we assume the same microstructure everywhere in Ω that allows considering a unique microscopic domain ω) as depicted in Fig. 1. The fluid is supposed incompressible and its viscosity is denoted by η.

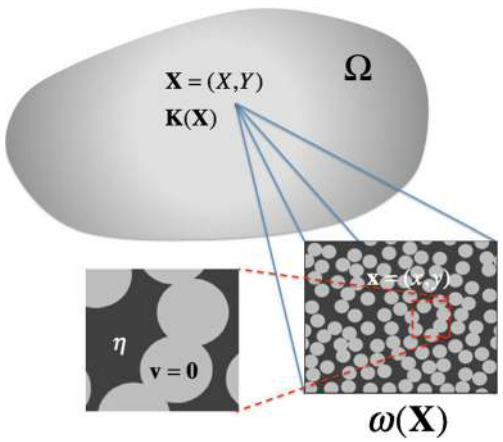

Fig. 1 Darcy (macro) and Stokes (micro) problems

At the macroscopic level the flow is described by the Darcy's law and continuity equation, that read

$$\begin{cases} \mathbf{V}(\mathbf{X}) = -\mathbf{K}(\mathbf{X}) \cdot \nabla P(\mathbf{X}) \\ \nabla \cdot \mathbf{V}(\mathbf{X}) = 0 \end{cases} \tag{4}$$

where $\mathbf{K}(\mathbf{X})$ is the "macroscopic" permeability tensor at position $\mathbf{X}$. In the light of the aforementioned assumption, $\mathbf{K}(\mathbf{X})$ is supposed to be the same everywhere, that is $\mathbf{K}(\mathbf{X}) \equiv \mathbf{K}$.

At the microscopic scale inclusions occupy the solid region ω_s assumed rigid and at rest, i.e. $\mathbf{v}(\mathbf{x} \in \omega_s) = \mathbf{0}$, separated by the fluid domain ω_f in which a Newtonian fluid, characterized by its viscosity η, flows. To be consistent with the Darcy's permeability definition (also called intrinsic or geometric permeability), it is supposed the fluid occupies all the volume between solid inclusions.

In [13] the postulated macroscopic Darcy's model was upscaled from the known microscopic Stokes' model by assuming that:

– There exists a localization tensor $\mathbf{M}(\mathbf{x}, \mathbf{X})$, which when the velocity $\mathbf{V}(\mathbf{X})$ is prescribed on the boundary of $\omega(\mathbf{X})$, $\partial\omega(\mathbf{X})$, the resulting velocity at each point $\mathbf{x} \in \omega(\mathbf{X})$, $\mathbf{v}(\mathbf{x})$, that comes from the solution of the resulting Stokes problem in $\omega(\mathbf{x})$, can be written from

$$\mathbf{v}(\mathbf{x}) \;=\; \mathbf{M}(\mathbf{x}, \mathbf{X}) \cdot \mathbf{V}(\mathbf{X}) \tag{5}$$

with $\langle \mathbf{v}(\mathbf{x}) \rangle = \mathbf{V}(\mathbf{X})$.

– The power dissipated at both scales must be the same for any velocity $\mathbf{V}(\mathbf{X})$, that results as proved in [13]

$$\langle 2\eta \mathbf{D} : \mathbf{D} \rangle \;=\; \nabla P(\mathbf{X}) \cdot \mathbf{V}(\mathbf{X}), \tag{6}$$

where $\mathbf{D}$ is the rate of strain tensor (symmetric component of the velocity gradient). Using the postulated macroscopic Darcy's law previous expression writes

$$2\eta \langle \mathbf{D} : \mathbf{D} \rangle \;=\; \mathbf{V}^T(\mathbf{X}) \cdot \mathbf{K}^{-1}(\mathbf{X}) \cdot \mathbf{V}(\mathbf{X}). \tag{7}$$

Introducing Eq. (5) in the left hand side of Eq. (7) and developing the contraction product, it results:

$$\langle \mathbf{D} : \mathbf{D} \rangle \;=\; \langle D_{ij} \cdot D_{ij} \rangle \;=\; \frac{1}{4} \langle \left(v_{i,j} + v_{j,i}\right) \cdot \left(v_{i,j} + v_{j,i}\right) \rangle, \tag{8}$$

with

$$v_i \;=\; M_{ik} \cdot V_k \tag{9}$$

with i = 1,2,3 and k = 1,2,3, in the general 3D case.

Thus, as soon as the localization tensor $\mathbf{M}$ is determined, from the macroscopic velocity $\mathbf{V}$ we can compute the microscopic one at each position $\mathbf{x}$ within the representative volume $\omega(\mathbf{X})$, $\mathbf{v}(\mathbf{x})$, and then evaluate the average of their derivatives according to Eq. 7 in order to identify $\mathbf{K}^{-1}$ and from it $\mathbf{K}$.

For calculating the localization tensor $\mathbf{M}(\mathbf{x}, \mathbf{X})$ in the general 3D case, three boundary value problems related to the Stokes' model in the microscopic domain $\omega(\mathbf{X})$ are solved:

$$\begin{cases} \nabla p^i(\mathbf{x}) = \eta \nabla^2 \mathbf{v}^i(\mathbf{x}) \\ \nabla \cdot \mathbf{v}^i(\mathbf{x}) = 0 \end{cases} \tag{10}$$

for three different boundary conditions on $\partial\omega(\mathbf{X})$ ($\partial\omega(\mathbf{X})$ is considered fully contained in the fluid phase, i.e. $\partial\omega(\mathbf{X}) \cap \overline{\omega}_s = \emptyset$):

$$\begin{cases} \mathbf{v}^1(\mathbf{x} \in \partial\omega(\mathbf{X})) = (1, 0, 0)^T \\ \mathbf{v}^2(\mathbf{x} \in \partial\omega(\mathbf{X})) = (0, 1, 0)^T \\ \mathbf{v}^3(\mathbf{x} \in \partial\omega(\mathbf{X})) = (0, 0, 1)^T \end{cases} \tag{11}$$

all of them kinematically admissible, i.e. they are compatible with the incompressibility constraint. Thus, the localization tensor $\mathbf{M}(\mathbf{x}, \mathbf{X})$ results finally:

$$\mathbf{M}(\mathbf{x}, \mathbf{X}) \;=\; \left(\mathbf{v}^1(\mathbf{x}) \quad \mathbf{v}^2(\mathbf{x}) \quad \mathbf{v}^3(\mathbf{x})\right) \tag{12}$$

Rheo-thinning nonlinear fluids

In the case of shear-thinning fluids the viscosity depends on the equivalent strain rate $\dot{\gamma}$, $\eta(\dot{\gamma})$, where

$$\dot{\gamma} = \sqrt{2\mathbf{D} : \mathbf{D}}, \tag{13}$$

with the strain-rate dependent viscosity expressed by the general form $\eta(\dot{\gamma})$.

The momentum and mass balances write

$$\begin{cases} \nabla p(\mathbf{x}) = \nabla \cdot (2\eta(\dot{\gamma})\mathbf{D}) \\ \nabla \cdot \mathbf{v}(\mathbf{x}) = 0 \end{cases} . \tag{14}$$

Once the solution of the nonlinear Stokes problem $\mathbf{v}(\mathbf{x})$ associated to the macroscopic velocity $\mathbf{V}(\mathbf{X})$ is obtained, its associated viscosity $\eta(\mathbf{x})$ is computed at each point of the microscopic domain and after freezing these values at each point $\mathbf{x} \in \omega(\mathbf{X})$ the three linear Stokes problems are solved

$$\begin{cases} \nabla p^i(\mathbf{x}) = \nabla \cdot \left(2\eta(\mathbf{x})\mathbf{D}^i\right) \\ \nabla \cdot \mathbf{v}^i(\mathbf{x}) = 0 \end{cases} \tag{15}$$

in $\omega(\mathbf{X})$ with the boundary conditions

$$\begin{cases} \mathbf{v}^1(\mathbf{x} \in \partial\omega(\mathbf{X})) = (1, 0, 0)^T \\ \mathbf{v}^2(\mathbf{x} \in \partial\omega(\mathbf{X})) = (0, 1, 0)^T \\ \mathbf{v}^3(\mathbf{x} \in \partial\omega(\mathbf{X})) = (0, 0, 1)^T \end{cases} \tag{16}$$

that allows defining the localization tensor from which the permeability can be identified as discussed in the case of linear fluids.

Nonlinear mico-macro solver

The permeability $\mathbf{K}(\mathbf{X})$ having been calculated at each $\mathbf{X}$, we come back to the macroscopic nonlinear Darcy's analysis. Thus, from the macroscopic velocity and pressure fields at iteration n (of the nonlinear iteration solver) $\mathbf{V}^n(\mathbf{X})$ and $P^n(\mathbf{X})$ the permeability tensor $\mathbf{K}^n(\mathbf{X})$ is computed from the microscopic analysis just described. Then, the macroscopic flow model reads

$$\nabla \cdot \left(\mathbf{K}^n(\mathbf{X}) \cdot \nabla P^{n+1}(\mathbf{X}) \right) = 0 \tag{17}$$

which solution gives the updated pressure $P^{n+1}(\mathbf{X})$ from which the updated velocity is computed:

$$\mathbf{V}^{n+1}(\mathbf{X}) = \mathbf{K}^n(\mathbf{X}) \cdot \nabla P^{n+1}(\mathbf{X}) \tag{18}$$

Now, the updated velocities $\mathbf{V}^{n+1}(\mathbf{X})$ are used to perform the new microscopic analysis allowing the update of the permeability tensor at each $\mathbf{X}$, $\mathbf{K}^{n+1}(\mathbf{X})$, and then the macroscopic calculation updates the macroscopic velocities and pressures. The iteration algorithm continues until reaching convergence.

Advanced nonlinear Stokes' solver

When considering a given representative microstructure, we could elaborate a parametric solution of the nonlinear flow problem in the microscopic volume ω by considering the velocities enforced on $\partial\omega$ as extra-coordinates within the PGD rationale [4, 11], i.e. calculating the parametric velocity field $\mathbf{v}(\mathbf{x}, \mathbf{V})$, with $\mathbf{x} \in \omega_f$ (part of ω occupied by the fluid) and $\mathbf{V} \in \mathcal{W}$ according to

$$\mathbf{v}(\mathbf{x} \in \omega_f, \mathbf{V} \in \mathcal{W}) \approx \sum_{n=1}^{Q} \mathbf{R}_n(\mathbf{x}) \circ \mathbf{S}_n(\mathbf{V}). \tag{19}$$

The nonlinear Stokes flow problem for a rheo-thinning fluid, reads:

$$\begin{cases} \nabla p = \nabla \cdot (2\eta(\dot{\gamma})\mathbf{D}) \\ \nabla \cdot \mathbf{v} = 0 \end{cases}. \tag{20}$$

At each iteration of the non-linear solver the equivalent rate of strain $\dot{\gamma}$ must be evaluated at each point and from it the viscosity $\eta(\mathbf{x} \in \omega_f)$. Then, expressing it in a separated form would enhance the efficiency of the separated representation solver [5]. The simplest way for performing such decomposition

$$\eta(\mathbf{x}, \mathbf{V}) = \sum_i F_i(\mathbf{x}) \cdot G_i(\mathbf{V}) \tag{21}$$

consists of using a singular value decomposition, even if more efficient possibilities exist, for example the ones based on the use of empirical interpolation [4] or cross approximations. It is always possible considering the separated representation of the velocity field without performing a separation of the strain-rate dependent fluid viscosity, route that implies costly numerical integrations.

A penalty formulation is used to circumvent the issue related to stable mixed formulations (LBB conditions) within the separated representation. It modifies the mass balance by introducing a penalty coefficient λ small enough as was successfully considered in our former works [1, 2, 9]

$$\nabla \cdot \mathbf{v} + \lambda\, p = 0, \tag{22}$$

or more explicitly

$$p = -\frac{\nabla \cdot \mathbf{v}}{\lambda} = -\frac{\mathrm{Tr}(\mathbf{D})}{\lambda}. \tag{23}$$

By replacing it into the momentum balance it comes

$$-\nabla \frac{\nabla \cdot \mathbf{v}}{\lambda} = \nabla \cdot (2\eta(\dot{\gamma})\mathbf{D}), \tag{24}$$

whose weak form, for a test velocity $\mathbf{v}^*$ vanishing in $\partial\omega$ (where the velocity will be prescribed), reads

$$\int_{\omega_f} \left\{ \frac{1}{\lambda} \mathrm{Tr}(\mathbf{D}^*)\mathrm{Tr}(\mathbf{D}) + 2\eta(\dot{\gamma})\mathbf{D}^* : \mathbf{D} \right\} d\mathbf{x} = 0, \tag{25}$$

that when addressing the parametric model is replaced by the extended weak form

$$\int_{\omega_f \times \mathcal{W}} \left\{ \frac{1}{\lambda} \mathrm{Tr}(\mathbf{D}^*)\mathrm{Tr}(\mathbf{D}) + 2\eta(\dot{\gamma})\mathbf{D}^* : \mathbf{D} \right\} d\mathbf{x}\, d\mathbf{V} = 0. \tag{26}$$

Now, the PGD solver proceeds as follows. We assume at iteration $q < Q$ the different functions involved in the separated representation of the velocity field $\mathbf{R}_n(\mathbf{x})$ and $\mathbf{S}_n(\mathbf{V})$, $n = 1, \cdots, q$, known (they have been already calculated), leading to the approximation

$$\mathbf{v}^q(\mathbf{x}, \mathbf{V}) = \sum_{n=1}^{q} \mathbf{R}_n(\mathbf{x}) \circ \mathbf{S}_n(\mathbf{V}). \tag{27}$$

At the present iteration the next functional couple $\mathbf{R}_{q+1}(\mathbf{x}) \circ \mathbf{S}_{q+1}(\mathbf{V})$ defining the $(q+1)$-approximation is looked for

$$\begin{aligned} \mathbf{v}^{q+1}(\mathbf{x}, \mathbf{V}) &= \sum_{n=1}^{q+1} \mathbf{R}_n(\mathbf{x}) \circ \mathbf{S}_n(\mathbf{V}) \\ &= \mathbf{v}^q(\mathbf{x}, \mathbf{V}) + \mathbf{R}_{q+1}(\mathbf{x}) \circ \mathbf{S}_{q+1}(\mathbf{V}). \end{aligned} \tag{28}$$

As both functions are unknown, the separated representation introduces a nonlinearity (even when solving a linear problem). Thus, a linearization procedure is compulsory. In general, and in this work in particular, the simplest schema is selected, an alternated directions fixed point algorithm that by assuming $\mathbf{S}_{q+1}(\mathbf{V})$ known (it is usually randomly initialized at the first iteration of the nonlinear solver), it computes $\mathbf{R}_{q+1}(\mathbf{x})$, and then from it $\mathbf{S}_{q+1}(\mathbf{V})$ is updated.

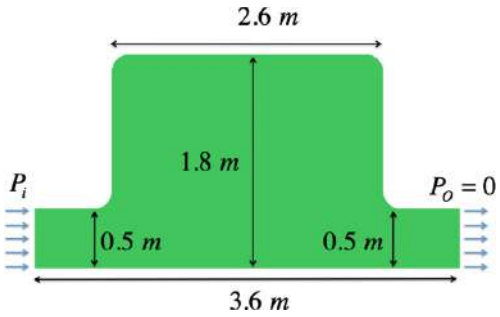

Fig. 2 Macroscopic flow geometry. Resin enters from the bottom left of the part and exits the part from the bottom right. Note that only the pressure is enforced on the inlet and outlet boundaries, so the flow intensity indicated in the figure does not correspond to the real velocity field existing on these boundaries that could differ from the uniform distribution here schematized

The iteration continues until reaching convergence, that is, the iteration fixed point.

When looking for $\mathbf{R}_{q+1}(\mathbf{x})$ the test function to be considered in the problem weak form (26) is $\mathbf{v}^* = \mathbf{R}^*(\mathbf{x}) \circ \mathbf{S}_{q+1}(\mathbf{V})$, whereas when looking for $\mathbf{S}_{q+1}(\mathbf{V})$ the test velocity reads $\mathbf{v}^* = \mathbf{R}_{q+1}(\mathbf{x}) \circ \mathbf{S}^*(\mathbf{V})$.

By introducing the approximation (28) and the test functions $\mathbf{v}^*(\mathbf{x}, \mathbf{V})$ into the problem weak form (26) it results a 3D boundary value problem – BVP – related to the calculation of the space function $\mathbf{R}_{q+1}(\mathbf{x})$ and a 3D algebraic problem when calculating the parametric function $\mathbf{S}_{q+1}(\mathbf{V})$.

As soon as the nonlinear iteration loop stops (when reaching the fixed point), we assume the solution approximated by the $(q+1)$-finite sum (28). The error can be evaluated by calculating the problem residual related to the tentative $\mathbf{v}^{q+1}(\mathbf{x}, \mathbf{V})$ as discussed in [5], and if it is still too large (with respect to a threshold small enough value

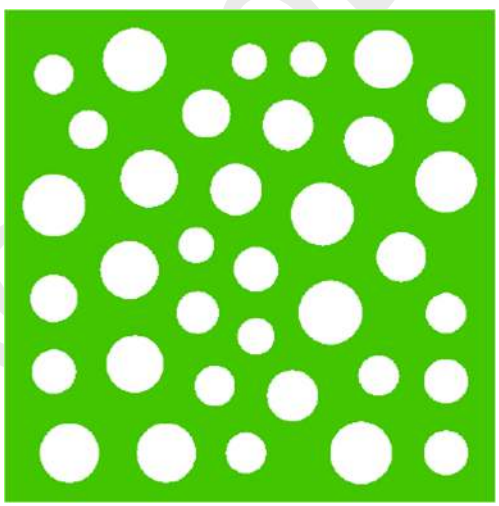

Fig. 3 Almost isotropic microstructure

Fig. 4 Orthotropic microstructure

specified by the user) the iteration continues and looks for the new functional couple $\mathbf{R}_{q+2}(\mathbf{x}) \circ \mathbf{S}_{q+2}(\mathbf{V})$ defining the solution approximation $\mathbf{v}^{q+2}(\mathbf{x}, \mathbf{V})$. The iteration enrichment loop continues until the residual becomes small enough. We assume that this occurs at iteration Q.

Thus, one can conclude that a sequence of 3D problems allows calculating the parametric solution of the velocity field $\mathbf{v}(\mathbf{x}, \mathbf{V})$. This number scales with Q, being slightly bigger because as just mentioned, for computing each functional couple we must solve a nonlinear problem that requires its own iteration loop.

When the PGD solver converges both the parametric velocity field $\mathbf{v}(\mathbf{x}, \mathbf{V}) \approx \mathbf{v}^Q(\mathbf{x}, \mathbf{V})$ and the associated parametric viscosity field $\eta(\mathbf{x}, \mathbf{V})$ are available. As previously discussed, the latter (even if it is not compulsory) is

Fig. 5 Representative volume superimposed and scaled to the macroscopic domain

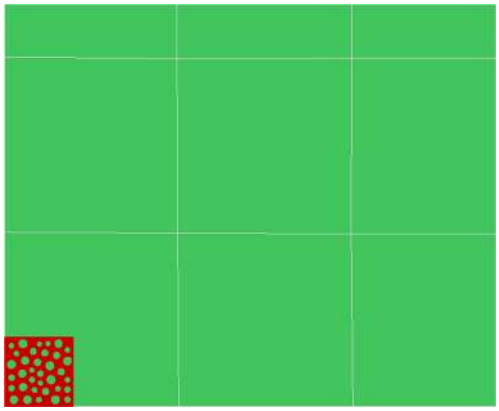

Fig. 6 Close-up of the representative volume superimposed and scaled to the macroscopic domain

preferable from the computational point of view to be expressed in a separated form

$$\eta(\mathbf{x}, \mathbf{V}) \approx \sum_{i=1}^{M} F_i(\mathbf{x}) \cdot G_i(\mathbf{V}). \tag{29}$$

As previously mentioned the localization tensor is determined by solving three BVP (in the general 3D case) related to the three unitary boundary conditions defined in Eq. (11). Now solving offline these BVP with the parametric viscosity $\eta(\mathbf{x}, \mathbf{V})$ given by Eq. (29) gives the three parametric velocity fields

$$\begin{cases} \mathbf{v}^1(\mathbf{x}, \mathbf{V}) \\ \mathbf{v}^2(\mathbf{x}, \mathbf{V}) \\ \mathbf{v}^3(\mathbf{x}, \mathbf{V}) \end{cases} \tag{30}$$

expressed in a separated form

$$\mathbf{v}^k(\mathbf{x}, \mathbf{V}) = \sum_{j=1}^{P^k} \mathbf{H}_\mathbf{j}^\mathbf{k}(\mathbf{x}) \circ \mathbf{W}_\mathbf{j}^\mathbf{k}(\mathbf{V}), \quad k = 1, 2, 3, \tag{31}$$

that allows calculating the different space derivatives involved in the velocity gradient used for evaluating the localization tensor and the resulting permeability, according to

$$\frac{\partial \mathbf{v}^k(\mathbf{x}, \mathbf{V})}{\partial x_l} = \sum_{j=1}^{P^k} \frac{\partial \mathbf{H}_\mathbf{j}^\mathbf{k}(\mathbf{x})}{\partial x_l} \circ \mathbf{W}_\mathbf{j}^\mathbf{k}(\mathbf{V}), \quad k = 1, 2, 3;\ l = 1, 2, 3. \tag{32}$$

By injecting these parametric expressions into the permeability definition, and after performing the integrals in space, the parametric permeability $\mathbf{K}(\mathbf{V})$ is obtained. As soon as the macroscopic velocity is known, it suffices particularizing it for such value of the macroscopic velocity to get the associated permeability.

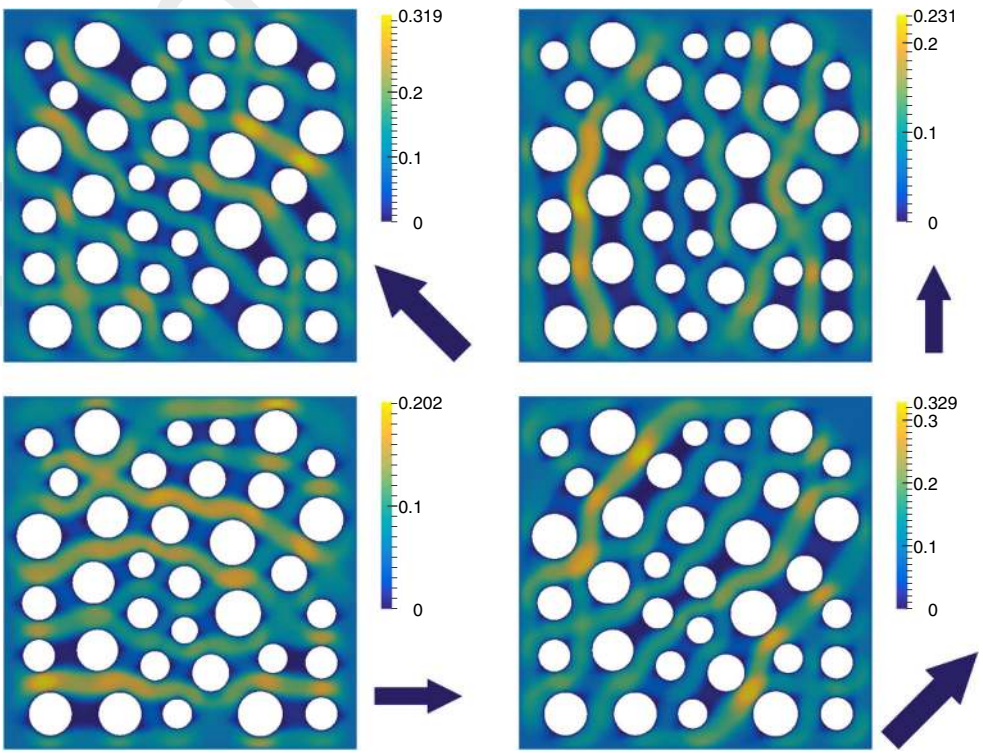

Fig. 7 $\mathbf{v}(\mathbf{x}, \mathbf{V})$ in the almost isotropic microstructure when particularizing if for four macroscopic velocities $\mathbf{V}$ indicated by the black arrows in the different cases

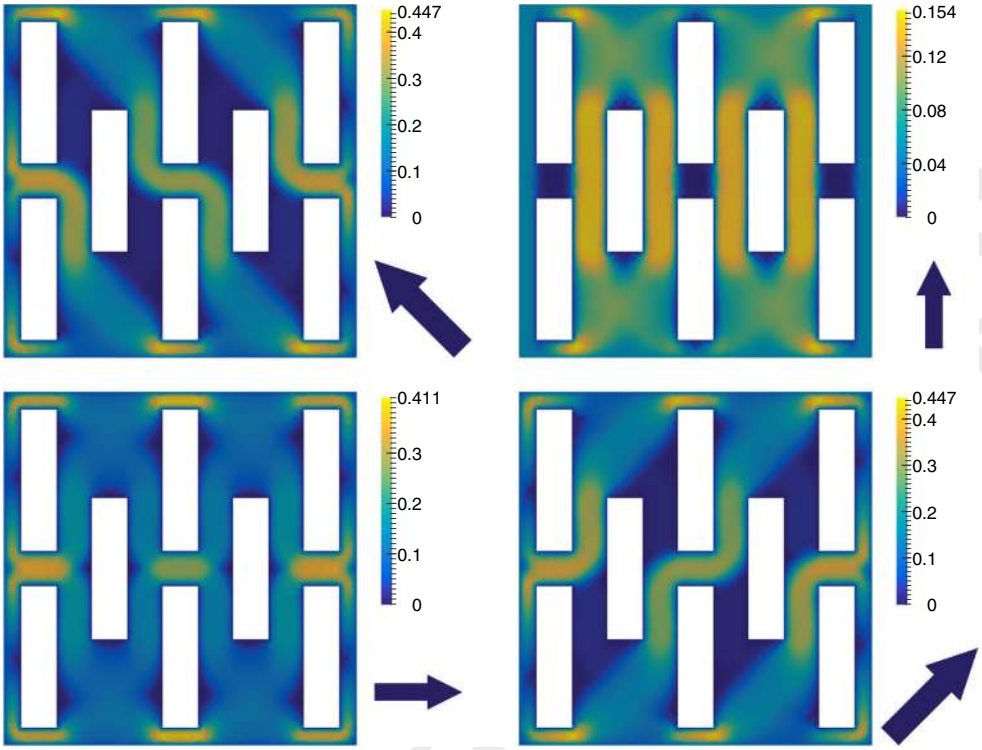

Fig. 8 $\mathbf{v}(\mathbf{x}, \mathbf{V})$ in the almost orthotropic microstructure when particularizing if for four macroscopic velocities $\mathbf{V}$ indicated by the black arrows in the different cases

Numerical results

In this section we consider the macroscopic domain depicted in Fig. 2, representing a composite part, assumed fully saturated by the fluid phase, and filled up with two possible types of porous microstructures, one almost isotropic and the other exhibiting a preferential directional behavior (orthotropic), both displayed respectively in Figs. 3 and 4. Figures 5 and 6 show a close-up of the macroscopic domain and the superimposed and scaled representative volume element in the case of the almost isotropic microstructure.

The size of the representative volumes are 2 cm $\times$ 2 cm. For the almost isotropic microstructure shown in Fig. 3 the porosity was 71.6 %, the average diameter of inclusions is 2 mm and characteristic distance between them of about 1 mm. A mesh consisting in 1977 elements was attached to the fluid domain ω_f, implying 21988 degrees of freedom. In the case of the orthotropic representative volume the size of rectangular inclusions depicted in Fig. 4 is 2 mm $\times$ 8 mm, with a characteristic distance between them of about 2 mm and a porosity of 68 %. The mesh in this case involves 1056 elements and 9394 degrees of freedom. All the finite elements are isoparametric Q2.

A mesh consisting in 1977 Q2-isoparametric elements involving 8125 degrees of freedom was associated to the macroscopic domain depicted in Fig. 2. A representative volume, all of them having the same microstructure, almost

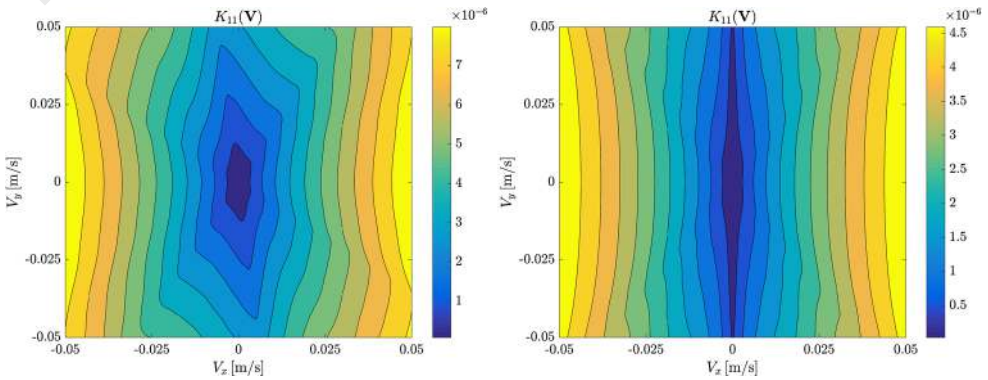

Fig. 9 $K_{11}(\mathbf{V})$ for the almost isotropic (*left*) and orthotropic (*right*) microstructures

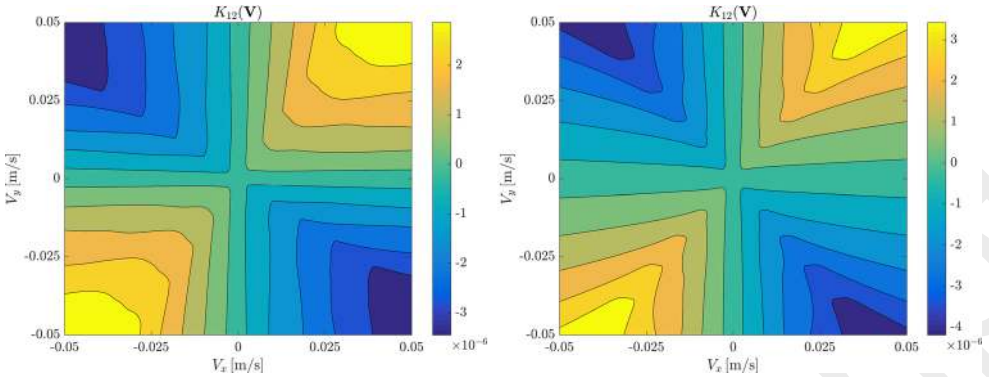

Fig. 10 $K_{12}(\mathbf{V})$ for the almost isotropic (*left*) and orthotropic (*right*) microstructures

isotropic or orthotropic, was attached to each Gauss point (each element involves 3×3 Gauss points).

Two different process conditions are considered by enforcing a high and low pressure drop between the inlet and the outlet $\Delta P = P_i - P_o$, $\Delta P = 10^3$ Pa and $\Delta P = 1.6\ 10^4$ Pa respectively, that are designated as low and high pressure conditions respectively. The higher pressure is meant to magnify the shear-thinning effects.

The rheo-thinning behavior of the fluid is described by the Carreau-Yasuda model, that is characterized by its viscosity at low and high shear rates η_0 and η_∞ respectively, and by three rheological coefficients a, n and τ, according to

$$\eta(\dot{\gamma}) = \eta_\infty + (\eta_0 - \eta_\infty)\left(1 + (\tau\dot{\gamma})^a\right)^{\frac{n-1}{a}} \tag{33}$$

The following material constants are used in the numerical simulations described below $\eta_0 = 1$ Pa $\cdot$ s, $\eta_\infty = 10^{-3}$ Pa $\cdot$ s, $n = 0.1$, $a = 5$ and $\tau = 1$ s. The procedure here described could be repeated for other fluid rheologies.

When constructing the parametric solution, that is $\mathbf{v}(\mathbf{x}, \mathbf{V})$, it is assumed that both components of the velocity vector can take values in the interval $(-V_{max}, V_{max})$, that means that the parametric domain $\mathcal{W}$ consists of a square of size $2V_{max}$, with $V_{max} = 5\ 10^{-2}$ m/s in the simulations. A mesh consisting in 1722 degrees of freedom was associated to $\mathcal{W}$.

The separated representation of the velocity field involves 250 terms in the almost isotropic microstructure whereas in the orthotropic one the number of modes reduces to 200. The solution procedure related to both parametric solutions requires 7 and 4 days of computation for the almost-isotropic and orthotropic microstructures respectively, using a standard laptop equipped of matlab. Even if this time seems a bit long, it is important to note that these solutions are computed only once and offline.

The parametric velocity fields of both microstructures were particularized in Figs. 7 and 8 to four different velocities prescribed on the representative volume boundary. These results only require particularizing the parametric velocity $\mathbf{v}(\mathbf{x}, \mathbf{V})$ associated in each microstructure (almost isotropic and orthotropic) for the four considered macroscopic velocities $\mathbf{V}$.

Figures 9, 10 and 11 compare the different components of the parametric permeability $\mathbf{K}(\mathbf{V})$, respectively $K_{11}(\mathbf{V})$, $K_{12}(\mathbf{V})$ and $K_{22}(\mathbf{V})$ for both microstructures.

Now, with the parametric permeability available for each possible value of the macroscopic velocity (in the range in which the parametric solution was constructed, i.e. $\mathbf{V} \in \mathcal{W}$), as soon as the macroscopic solution procedure requires at

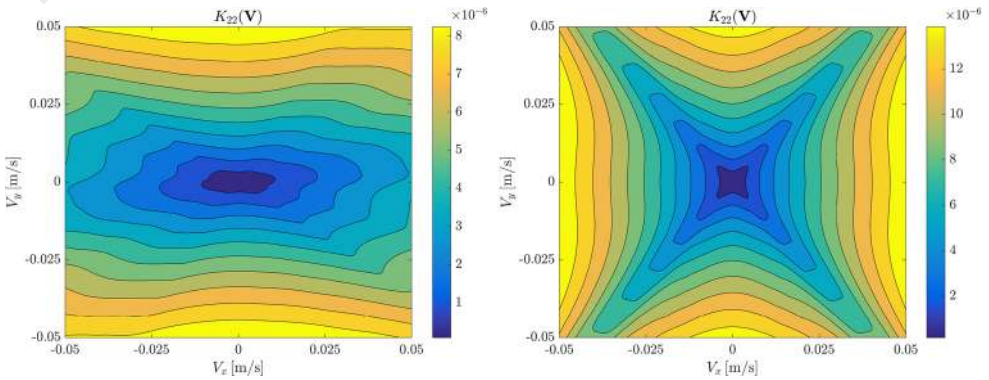

Fig. 11 $K_{22}(\mathbf{V})$ for the almost isotropic (*left*) and orthotropic (*right*) microstructures

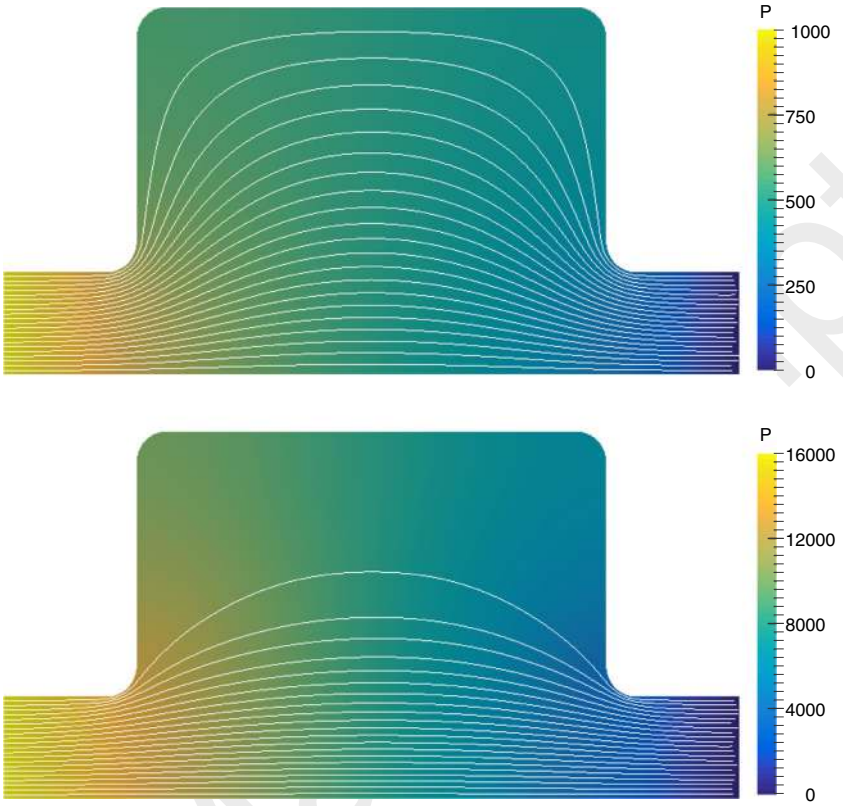

Fig. 12 Pressure field $P(\mathbf{X})$ for the almost isotropic microstructure when applying low (top) and high (bottom) pressure drop between the inlet and the outlet. Solid lines are streamlines

iteration n of the nonlinear solver the value of permeability in a certain point $\mathbf{X} \in \Omega$, where the tentative velocity $\mathbf{V}^n(\mathbf{X})$ results from the tentative permeability at the previous iteration $\mathbf{K}^{n-1}$ from the Darcy's law $\mathbf{V}^n(\mathbf{X}) = \mathbf{K}^{n-1} \cdot \nabla P^n(\mathbf{X})$,

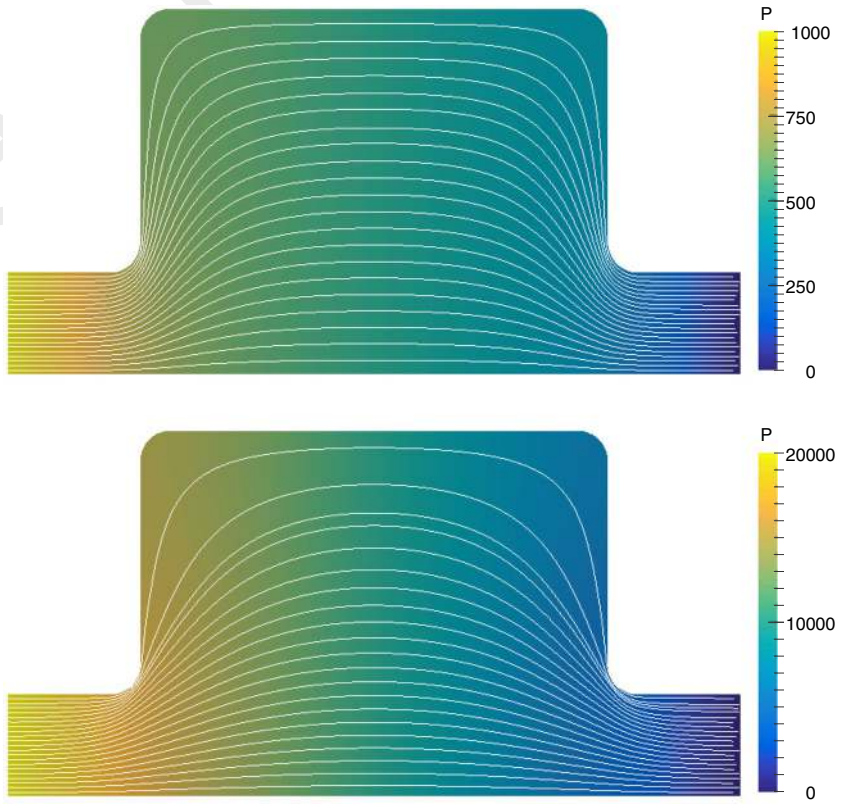

Fig. 13 Pressure field $P(\mathbf{X})$ for the orthotropic microstructure when applying low (top) and high (bottom) pressure drop between the inlet and the outlet. Solid lines are streamlines

Fig. 14 Permeability tensor trace $\mathrm{Tr}(\mathbf{K})$ at each point $\mathbf{X} \in \Omega$ for the almost isotropic microsctructure when applying high pressure drop between the inlet and the outlet

with $\mathbf{K}^{n-1} = \mathbf{K}(\mathbf{V}^{m-1}(\mathbf{X}))$, the calculation of the new permeability at that point $\mathbf{X}$ and for that velocity $\mathbf{V}^n$ only requires particularizing the parametric permeability for that value of the macroscopic velocity $\mathbf{V}^n$.

The solution on a state-of-the-art laptop equipped with Matlab requires 0.15 s for solving the macroscopic linear flow problem, whereas each iteration involved in the solution of the macroscopic nonlinear flow problem requires 0.2 s.

Figures 12 and 13 depict the pressure field for both microstructures and both pressure drop conditions. These figures show significant difference in terms of magnitude and distribution of pressure, as well as on streamlines. They clearly show the influence of both the flow intensity and the microstructure.

Figure 14 depicts the resulting trace of the permeability tensor $\mathrm{Tr}(\mathbf{K}) = K_{11} + K_{22}$ at each point $\mathbf{X} \in \Omega$ for the almost isotropic microsctructure when applying high pressure drop between the inlet and the outlet. When applying the low pressure drop the permeability was found almost constant all along the domain Ω, however when considering the high pressure drop, the involved shear rates at the microscopic scale induce a drop in viscosity that increases the effective permeability. We can notice in Fig. 14 that the resulting permeability in Ω ranges in an interval covering to order of magnitude. Moreover, it can be also noticed that the drop in viscosity induces the expected flow localization, where the almost equi-distributed streamlines in the case of low pressure drop tend to localize in the region of higher permeability as soon as the pressure (and the associated flow rate) becomes high enough.

When solving the macroscopic flow problem in both microstructures for different pressure drops, the resulting flow rates follow (see Figs. 15 and 16) a linear evolution in the case of a linear fluid, and the expected nonlinear evolution when considering the rheo-thinning behavior previously described.

Linear flow results when considering the constant fluid viscosity given by η_0 and the permeability $\mathbf{K}(\mathbf{V} \approx \mathbf{0})$. In these simulations the flow behavior in the linear case was

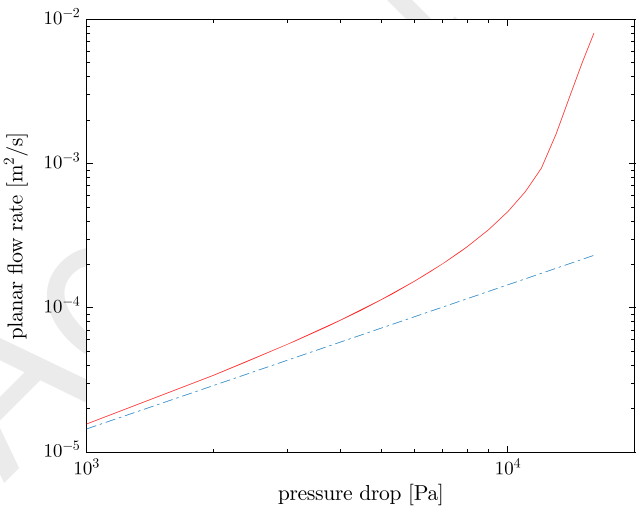

Fig. 15 Pressure drop versus the resulting flow rate for the almost isotropic microstructure for linear and nonlinear fluids

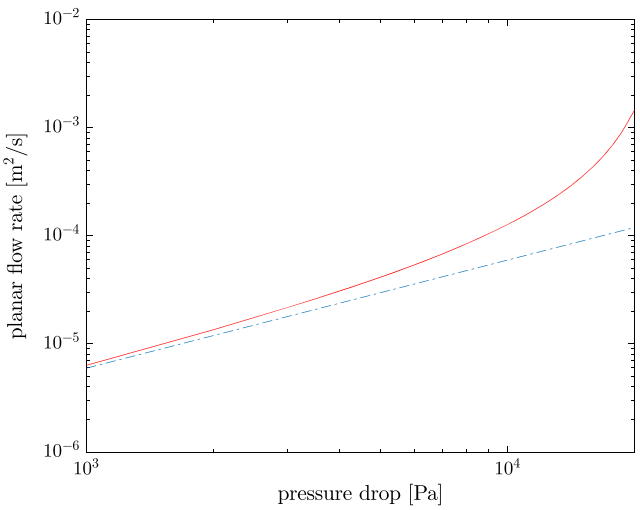

Fig. 16 Pressure drop versus the resulting flow rate for the orthotropic microstructure for linear and nonlinear fluids

found to be very close to the one obtained when enforcing the lowest pressure drop, i.e. $\Delta P = 10^3$ Pa.

Conclusions

This paper discussed the definition of a permeability tensor for linear and nonlinear fluids flowing in two-scale porous media. The upscaling procedure is based on the existence of a localization tensor and the equality of dissipated powers at the different scales.

In the case of linear fluids an equivalent geometrical permeability tensor can be defined at the macroscopic scale, and it only depends on the microscopic geometrical features. It can be calculated offline (for a given microstructure) by solving 3 BVP. On the contrary when considering nonlinear fluids the permeability is no longer purely geometric.

In order to speed up macroscopic calculation, it is proposed to construct parametric solutions of microscopic flow problems defined in a representative volume with a given microstructure. As soon as the permeability is expressed with a parametric dependence on the macroscopic velocity, its particularization becomes computationally very fast, making possible the solution of the macroscopic flow problem with a computational complexity that scales with the number of iterations needed by the nonlinear macroscopic solution procedure.

References

1. Aghighi S, Ammar A, Metivier C, Normandin M, Chinesta F (2013) Non incremental transient solution of the Rayleigh-Bénard convection model using the PGD. J Non-Newtonian Fluid Mech 200:65–78
2. Aghighi MS, Ammar A, Metivier C, Chinesta F Parametric solution of the Rayleigh-Bénard convection model by using the PGD: Application to nanofluids. Int J Numer Methods Heat Fluid Flow. In press
3. Chinesta F, Ammar A, Lamarchand F, Beauchene P, Boust F (2008) Alleviating mesh constraints: Model reduction, parallel time integration and high resolution homogenization. Comput Methods Appl Mech Eng 197:400–413
4. Chinesta F, Leygue A, Bordeu F, Aguado JV, Cueto E, Gonzalez D, Alfaro I, Ammar A, Huerta A (2013) A. PGD-based computational vademecum for efficient design, optimization and control. Arch Comput Meth Eng 20(1):31–59
5. Chinesta F, Keunings R, Leygue A (2013) The Proper Generalized Decomposition for Advanced Numerical Simulations. A primer. Springerbriefs, Springer
6. Chinesta F, Huerta A, Rozza G, Willcox K (2016) Model Order Reduction. In: Erwin Stein, René de Borst, Tom Hughes (eds) Encyclopedia of Computational Mechanics. Second Edition. John Wiley & Sons, Ltd., New York
7. Donea J, Huerta A (2003) Finite element methods for flow problems. Wiley
8. Geers MGD, Kouznetsova VG, Brekelmans WAM (2010) Multiscale computational homogenization: Trends and challenges. J Comput Appl Math 234(7):2175–2182
9. Ghnatios Ch, Chinesta F, Binetruy Ch The squeeze flow of composite laminates. Int J Mater Form. In press
10. Gunes H, Sirisup S, Em Karniadakis G (2006) Gappy data: To Krig or not to Krig? J Comput Phys 212:358–382
11. Lamari H, Ammar A, Cartraud P, Legrain G, Jacquemin F, Chinesta F (2010) Routes for efficient computational homogenization of non-linear materials using the proper generalized decomposition. Arch Comput Meth Eng 17(4):373–391
12. Lopez E, Abisset-Chavanne E, Lebel F, Upadhyay R, Comas-Cardona S, Binetruy C, Chinesta F Advanced thermal simulation of processes involving materials exhibiting fine-scale microstructures. Int J Mater Form. In press
13. Lopez E, Abisset-Chavanne E, Comas-Cardona S, Binetruy et C, Chinesta F Flow modeling of linear and nonlinear fluids in two and three scale fibrous fabrics. In press
14. Nguyen VP, Stroeuen M, Sluys LJ (2011) Multiscale continous and discontinous modeling of heterogeneous materials: a review on recent developments. J Multiscale Model 03: 229
15. Ponte Castañeda P., Suquet P (1998) Nonlinear composites. Adv Appl Mech 34:171–302